Electrogeneration of Single Nanobubbles at Sub-50-nm-Radius Platinum Nanodisk Electrodes

ARTICLE *in* LANGMUIR · AUGUST 2013

Impact Factor: 4.46 · DOI: 10.1021/la402496z · Source: PubMed

Langmuir

Article

pubs.acs.org/Langmuir

Electrogeneration of Single Nanobubbles at Sub-50-nm-Radius Platinum Nanodisk Electrodes

Long Luo and Henry S. White*

Department of Chemistry, University of Utah, 315 S 1400 E, Salt Lake City, Utah 84112, United States

Supporting Information

ABSTRACT: The electrochemical generation of individual H_2 nanobubbles at Pt nanodisk electrodes immersed in a 0.5 M H_2SO_4 solution is reported. A sudden drop in current associated with the transport-limited reduction of protons is observed in the $i-V$ response at Pt nanodisk electrodes with radii of less than 50 nm. This decrease in current (~95% blockage) corresponds to the formation of a single H_2 nanobubble attached to the nanoelectrode that blocks proton transport to the surface. The current at which nanobubble formation occurs, i_{nb}^{P}, is independent of scan rate and H_2SO_4 concentration (for $[H_2SO_4] > 0.1$ M), indicating a critical concentration profile of electrogenerated H_2 required to nucleate a nanobubble. Finite element simulation based on Fick's first law, combined with the Young–Laplace equation and Henry's law, indicates that the concentration of H_2 near the nanoelectrode surface at i_{nb}^{P} exceeds the saturation concentration necessary to generate a nanobubble with a size comparable to the electrode size. The rapid dissolution of the nanobubble due to the high inner Laplace pressure is precisely balanced by the electrogeneration of H_2 at the partially exposed Pt surface, resulting in a dynamically stabilized nanobubble. Preliminary measurements of the $i-t$ response during nanobubble formation indicate a two-step nucleation and growth mechanism with time scales on the order of 100 μs (or less) and ~1 ms, respectively.

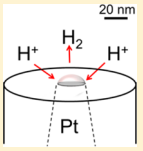

INTRODUCTION

Research on interfacial nanobubbles has greatly advanced during the past decade, including the development of new methods of generating[1−3] and detecting nanobubbles[4−15] as well as the development of the theory and mechanism of nanobubble formation and stabilization.[16−20] At present, it is possible to generate large ensembles of nanobubbles of different gas types at hydrophobic surfaces (e.g., perfluorodecyltrichlorosilane and highly orientated hydrophobic pyrolytic graphite) using the solvent exchange technique[4] or the electrolysis of water.[1] Interfacial nanobubbles have been observed and characterized by tapping-mode atomic force microscopy (TMAFM).[4−13] In recent experimental reports, interfacial nanobubbles were found to exist for hours or days, in contrast to the expected short lifetime due to rapid gas dissolution.[21] Several mechanisms have been proposed to explain the observed long lifetime of nanobubbles, including the role of impurities at the interface,[18,22,23] dynamic steady state,[3,17] and contact line pinning,[16,20] but still no general agreement has yet been reached for the actual mechanism. Not only is the stabilization mechanism under debate but also the mechanism of nanobubble formation remains unclear. It has been proposed that interfacial nanobubbles result from a supersaturation of gas at the interface.[16,24] A quartz crystal microbalance study by Zhang et al. suggests that this process occurs in less than ~1 min.[25] However, Seddon et al.[26] and Dong et al.[27] recently reported the formation of surface nanobubbles in solutions that were not supersaturated by the corresponding gas. How nanobubbles form at the interface and why they remain stable are still open questions.

In this Article, we present a new approach for investigating the formation and stability of a nanobubble. Instead of generating a large ensemble of nanobubbles at a macroscopic surface, a Pt nanodisk electrode is used to electrochemically generate a single H_2 nanobubble by reducing protons in a strong sulfuric acid solution (Scheme 1). The nanoscale dimension of the nanoelectrode itself provides exquisite sensitivity for detecting small changes near or at the electrode surface,[28−31] while fast electrochemical measurements allow the study of the dynamics of nanobubble formation. High spatial and time resolutions make the nanodisk electrode a powerful platform for studying the formation and stabilization of nanobubbles. As detailed below, the formation of a single nanobubble at the Pt nanodisk electrode can be readily detected from the current drop in the reduction of H^+ caused by the blockage of the electrode surface. Our results suggest that a critical H_2 concentration profile near the nanoelectrode

Scheme 1. Schematic Representation of the Electrochemical Formation of an Individual Nanobubble at a Pt Nanodisk Electrode with a Radius of a < 50 nm[a]

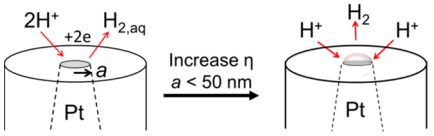

[a]The Pt nanodisk is shrouded in glass. The hemispherical shape of the nanobubble is drawn here for schematic purposes and is unlikely to represent the actual shape.

Received: July 1, 2013
Revised: August 5, 2013
Published: August 5, 2013

surface is required to initiate nanobubble formation. Additionally, rapid $i-t$ recording of the current drop provides insight into the dynamics of nanobubble formation, whereas the measurement of the residual current after the formation of a nanobubble provides insight into the mechanism by which a nanobubble remains stable. We demonstrate that a residual current of several hundred picoamps, corresponding to H_2 electrogeneration at the Pt/gas/liquid interface, balances the rate of H_2 dissolution from the nanobubble.

EXPERIMENTAL SECTION

Chemicals. Sulfuric acid (98%, ACS grade, EMD) was used as received. All aqueous solutions were prepared using water (18 MΩ·cm) from a Barnstead E-pure H_2O purification system.

Nanodisk Electrode Fabrication and Characterization. Platinum nanodisk electrodes were fabricated according to previously reported procedures from our laboratory.[32] Briefly, a polycrystalline Pt wire attached to a W rod was electrochemically sharpened in a NaCN solution and then sealed in a glass capillary (Dagan Corp., Prism glass capillaries, SB16, 1.65 mm outer diameter, 0.75 mm inner diameter, softening point 700 °C) using a H_2/air flame. The capillary was then polished with silicon carbide polishing papers (400 grit/p800 to 1200 grit/p4000) until a Pt nanodisk was exposed, as indicated by the use of an electronic feedback circuit.[32] The radii of the resulting nanodisks, a, were determined from the voltammetric steady-state diffusion-limited current, i_d, for the oxidation of 5 mM ferrocene (Fc) dissolved in acetonitrile containing 0.1 M tetrabutylammonium hexafluorophosphate ($TBAPF_6$). The radii were calculated using the equation

$$i_d = 4nFDC^*a \quad (1)$$

where a is the radius of the nanodisk electrode, D (2.5×10^{-5} cm^2/s[32]) and C^* are the diffusion coefficient and the bulk concentration of Fc, respectively, and n is the number of electrons transferred per molecule (in this case, equal to 1). The experimental steady-state voltammograms used to measure the electrode radii are presented in the SI file.

Electrochemical Apparatus. A Dagan Cornerstone Chem-Clamp potentiostat and a Pine RDE4 (used as the waveform generator) were interfaced to a computer through a PCI data acquisition board (National Instruments) to collect the $i-V$ and $i-t$ data. The current from the Dagan potentiostat was passed through a 10 kHz low-pass filter. For currents >100 nA using larger Pt disk electrodes, the Pine RDE 4 was used alone as the potentiostat/programmer. $i-V$ curves were recorded with virtual instrumentation written in LabVIEW (National Instruments) at a data acquisition rate of 150 kHz. A Ag/AgCl (3 M NaCl) electrode was used as the counter/reference electrode.

Finite Element Simulation. The finite element simulations were performed using COMSOL Multiphysics 3.5 (Comsol, Inc.) on a high-performance desktop PC. The simulation geometry, mesh, and boundary conditions are provided in the SI file.

RESULTS AND DISCUSSION

Electrochemical Formation of a Single Nanobubble. Figure 1a shows a typical cyclic voltammogram (CV) recorded at a 27-nm-radius Pt nanodisk electrode immersed in deoxygenated 0.5 M H_2SO_4 (scan rate = 100 mV/s). The H_2SO_4 solution was deoxygenated by bubbling the solution with N_2 for about half an hour. At potentials positive of −0.25 V versus Ag/AgCl, the voltammogram displays very small currents (<10 pA) resulting from the double-layer capacitance and the absorption/desorption of hydrogen and oxygen species at the Pt surface.[33,34] As the voltage is scanned negative of −0.25 V, corresponding to the thermodynamic potential for the reduction of protons ($E^0_{(H^+/H_2)}$), the current increases rapidly until it reaches a peak value, i^P_{nb}, at ∼−0.4 V versus Ag/AgCl.

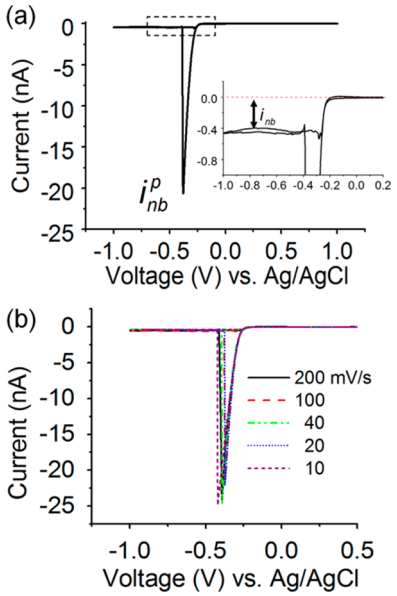

Figure 1. (a) Cyclic voltammogram recorded for a 27-nm-radius Pt electrode immersed in a deoxygenated 0.5 M H_2SO_4 solution (scan rate = 100 mV/s). The transport-limited current associated with the electroreduction of H^+ drops suddenly at ∼−0.4 V versus Ag/AgCl because of the nucleation and rapid growth of a H_2 nanobubble. The peak current at which nanobubble formation occurs is labeled as i^P_{nb}. The inset shows a residual current i_{nb} of −0.4 nA after the formation of a nanobubble. (b) Cyclic voltammetric response for the same 27-nm-radius Pt electrode recorded at scan rates ranging from 10 to 200 mV/s.

Within this range, the $i-V$ response is smooth and continuous, indicating no bubble formation. For the 27-nm-radius electrode, the i^P_{nb} of ∼−21 nA (negative sign denotes a cathodic current) is approximately 20% of the predicted proton-diffusion-limited current, i_d = −97 nA (eq 1, using a = 27 nm, $D_{H^+} = 9.3 \times 10^{-5}$ cm^2/s,[35] and C^* = 1 M). After passing through the peak current, the current decreases to a residual current value i_{nb} of ∼−450 pA. We interpret this voltammetric response as corresponding to the formation of a single nanobubble at the 27-nm-radius Pt disk that blocks a large fraction (>95%) of the active electrode surface. The inset in Figure 1 shows an enlargement of the residual current following nanobubble formation. The observation of a residual current for H^+ reduction suggests that the nanobubble at the electrode is in a dynamic steady state in which electrolytically generated H_2 flows into the nanobubble and balances the diffusion of H_2 at the nanobubble/liquid interface (Scheme 1).

On the reverse voltammetric scan from −1.0 V toward positive potentials (at scan rates of up to 1 V/s), we did not observe an anodic peak at potentials positive of $E^0_{(H^+/H_2)}$ corresponding to the oxidation of the H_2 nanobubble or H_2 dissolved in the solution. This result suggests that the H_2 bubble dissolves rapidly on the voltammetric time scale as soon as H^+ is no longer being reduced. The diffusion of dissolved H_2 away from a 27-nm-radius electrode is too rapid to allow its detection at the scan rates used in this study.

Figure 1b shows that the CV response, including the value of the peak current, i^P_{nb}, is essentially independent of the scan rate between 10 and 200 mV/s. Prior to nanobubble formation, the current is limited by a combination of H^+ transport and reduction kinetics at the nanoelectrode.[36,37] When the current

dx.doi.org/10.1021/la402496z | Langmuir 2013, 29, 11169−11175

reaches the critical value of ∼−21 nA, it drops rapidly, indicating a fast nanobubble formation process. The $i-V$ response of an 11-nm-radius nanodisk electrode exhibits a very similar scan-rate-independent response with $i_{nb}^{p} \approx -10$ nA (SI file). Voltammograms corresponding to the formation of H_2 nanobubbles were reproducible over multiple scans between 1 and −1 V versus Ag/AgCl, suggesting that bubble formation did not significantly damage the Pt surface.

To investigate the dynamics of nanobubble formation, we recorded the $i-t$ of the 27-nm-radius Pt nanodisk while scanning the electrode potential from 1 to −1 V at a scan rate of 100 mV/s (Figure 2). The expansion of the $i-t$ trace (Figure 2b) clearly shows that the $i-t$ response is described by two time constants, with more than 50% of the current decrease occurring during the first 200 μs and then a slower decay (to the steady-state value of ∼−1 nA) occurring in a few milliseconds. This response suggests a two-step mechanism of nanobubble formation. Note that the potentiostat temporal resolution is limited by a 10 kHz low-pass filter (Experimental Section); thus, the time constant for the first step is probably shorter than the ∼100 μs time scale observed in the measurement.

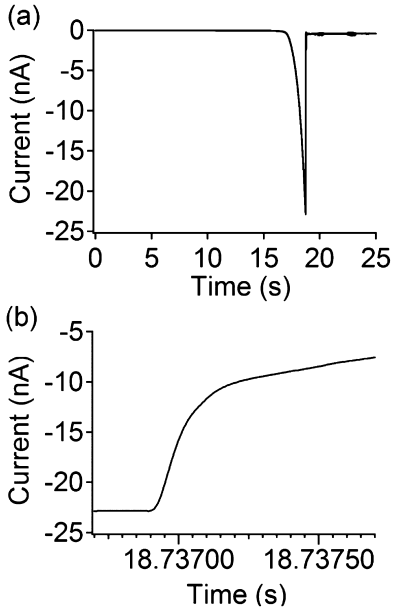

Figure 2. (a) $i-t$ trace recorded while scanning the voltage at 100 mV/s from 1 to −1 V at the 27-nm-radius Pt nanodisk immersed in 0.5 M H_2SO_4. (b) Expansion of the trace in part (a) showing that the formation of a nanobubble is described in a two-step mechanism, with the initial step occurring on a time scale of a few hundred microseconds, followed by a slower growth process on the time scale of a few milliseconds. In this particular example, the current reaches the steady-state residual value, i_{nb}, in ∼3 ms. The temporal resolution of the measurement is limited by the instrumental 10 kHz bandwidth.

Possible Mechanism of Electrochemically Nanobubble Formation. The $i-t$ response suggest a two-step formation of a nanobubble when the current reaches i_{nb}^{p}. We hypothesize that the H_2 concentration at the nanoelectrode surface is sufficiently high to nucleate a nanobubble at the Pt nanodisk surface when the current reaches i_{nb}^{p}, representing the first step. After the nucleation step, the nanobubble grows more slowly to near cover the Pt nanodisk, leading to a further decrease in current. The finding that the current for H^+ reduction does not completely vanish indicates that the Pt nanodisk is not completely covered by the nanobubble.

To test this hypothesis, we performed finite element simulations to obtain the concentration profile of electrochemically generated H_2 at the critical current i_{nb}^{p}. Assuming the system is at steady state, the flux of H_2 ($\mathbf{J}_{out,H_2}$) away from the nanodisk should be equal to half of the electron-transfer flux at the nanodisk electrode (the latter is equal to the influx of H^+ to the nanodisk electrode). The integral of the electron flux over the nanodisk surface is recorded as the critical current i_{nb}^{p} (eq 2), and $\mathbf{J}_{out,H_2}$ is governed by Fick's first law (eq 3). Finite element simulation using the Newton−Raphson method was employed to solve the following two equations from an appropriate initial guess. Details including the mesh, geometry, and boundary conditions are given in the SI file.

$$i_{nb}^{p} = 2F \int \mathbf{J}_{out,H_2} \cdot \mathbf{n}\, ds \tag{2}$$

$$\mathbf{J}_{out,H_2} = -D_{H_2} \nabla c_{H_2} \tag{3}$$

Figure 3 shows the simulated H_2 distribution near a 27-nm-radius nanodisk electrode at the critical current i_{nb}^{p} of −21 nA.

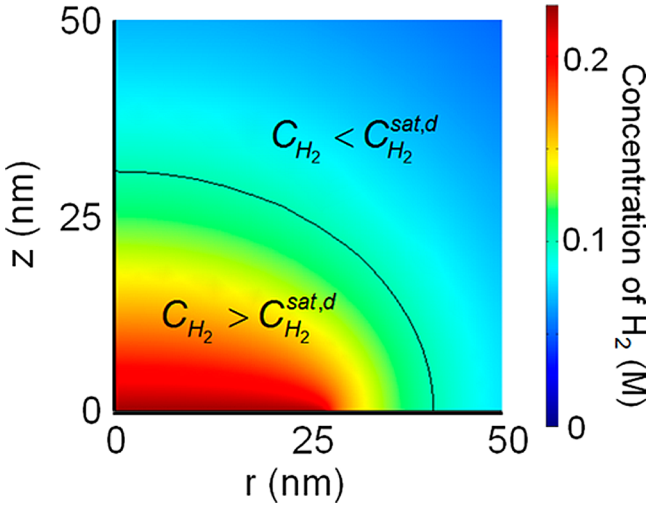

Figure 3. Simulated H_2 distribution (surface) near a 27-nm-radius Pt nanodisk at the experimentally measured critical current i_{nb}^{p} of −21 nA. The black line is the 0.1 M H_2 contour line, within which the concentration of H_2 (C_{H_2}) is higher than the saturation concentration $C_{H_2}^{sat,d}$ (∼0.10 M, see text) required to form a spherical nanobubble with a diameter of 20 nm.

The concentration of H_2 near the electrode greatly exceeds the saturation concentration of H_2 at 1 atm and room temperature (∼0.8 mM[38]). The black line corresponds to the 0.1 M H_2 contour line, within which the concentration of H_2 is sufficiently large to be in equilibrium (via Henry's law, eq 5) with a 20-nm-diameter spherical nanobubble sitting on the electrode. More specifically, the Young−Laplace equation (eq 4) correlates the internal pressure of a nanobubble (p_{nb}) with its radius (r_{nb}) while Henry's law (eq 5) provides the equilibrium concentration ($C_{H_2}^{s}$) at the nanobubble/liquid interface at that pressure.

dx.doi.org/10.1021/la402496z | Langmuir 2013, 29, 11169−11175

$$\Delta p = p_{nb} - p_{out} = \frac{2\gamma}{r_{nb}} \quad (4)$$

$$\Delta p = p_{nb} - p_{out} = kC^{s}_{H_2} \quad (5)$$

The Henry's law constant k = 1.43 atm/mM is taken from the experimental results from Wiebe et al.[39] γ is the surface tension of the sulfuric acid solution (0.073 N/m),[40] and p_{out} is the pressure of the bulk solution. Thus, for a 20-nm-diameter spherical nanobubble, the inner pressure, p_{nb}, is calculated to be ~144 atm and $C^{s}_{H_2}$ is calculated to be ~0.10 M.

After the nucleation of a nanobubble, the nanobubble grows and is pinned at the circumference between the Pt and glass because of the difference in hydrophobicity of these two materials. As demonstrated below, the observation that the residual current is as low as a few hundred picoamps suggests that the H_2 nanobubble covers the majority of the active electrode surface. A clean Pt surface has been reported by Woods et al. to be hydrophilic in sulfate media (Na_2SO_4) at all potentials between hydrogen and oxygen evolution.[41] However, the hydrophilicity of Pt is sensitive to surface crystallography[42] and absorbed molecules.[43] In the absence of extensive cleaning, contact angles on Pt electrodes generally indicate a hydrophobic surface.[43]

In summary, we believe that the nucleation and formation of a nanobubble occurs when the H_2 generated by the reduction of H^+ exceeds a saturation H_2 concentration that corresponds to a bubble of size equal to the dimension of the nanodisk electrode. This is also supported by the finding that $i^{P}_{nb} \approx -10$ nA at an 11-nm-radius electrode, corresponding to a H_2 concentration of ~0.27 M at the electrode surface, a value sufficiently high to form a 10-nm-diameter spherical nanobubble.

Concentration Dependence. According to the above-proposed mechanism, nanobubble formation occurs from a supersaturation of H_2 when the current reaches a sufficiently large value, i^{P}_{nb}. Because the maximum available current at a nanoelectrode in the absence of the nanobubble formation is limited by the diffusive flux of protons, we further tested our proposed mechanism by varying the H_2SO_4 concentration and thus the maximum available current (eq 1).

Figure 4 shows the cyclic voltammetric responses at a 27-nm-radius Pt nanodisk as a function of H_2SO_4 concentration: (a) 0.01 to 0.05 M and (b) 0.1 to 0.5 M. The shape of the $i-V$ response transforms gradually from a sigmoidal-shaped wave to a peak-shaped response as the concentration is increased from 0.01 to 0.5 M. A mixture of sigmoidal and peak features is present at 0.1 M, where the theoretical proton-diffusion-limited current is ~−19.4 nA, slightly smaller than the critical current i^{P}_{nb} of ~−21 nA. When the H_2SO_4 concentration is greater than ~0.1 M, a peak-shape response with a concentration-independent i^{P}_{nb} is observed, indicating a critical concentration profile. In contrast, for H_2SO_4 concentrations <0.1 M, the conventional diffusion-limited sigmoidal response at a nanodisk electrode results from the failure to achieve the supersaturation of H_2. Similar behavior is observed at an 11-nm-radius Pt nanodisk electrode (SI file).

Size Dependence. Figure 5 shows the cyclic voltammetric response as a function of the Pt nanodisk radius in 0.5 M H_2SO_4. For nanodisks with radii <50 nm, a peak shape voltammetric response is observed that is similar to that detailed above, whereas for radii >50 nm the voltammetric response is sigmoidal-shaped with significant hysteresis in the forward and reverse scans. The maximum current of the sigmoidal-like response is close to the diffusion-limited current. For example, a 226-nm-radius nanodisk yielded a maximum current of −770 nA, in good agreement with the calculated proton-diffusion-limited current of −810 nA (eq 1). Using a similar finite element simulation method as described above, the concentration profile of H_2 for the 226-nm-radius nanodisk at the maximum current was computed (SI file). The resulting profile shows that the H_2 concentration near the surface is as high as 0.6−0.8 M, and according to Henry's law (eq 5) and the Young−Laplace equation (eq 4), such a concentration is able to

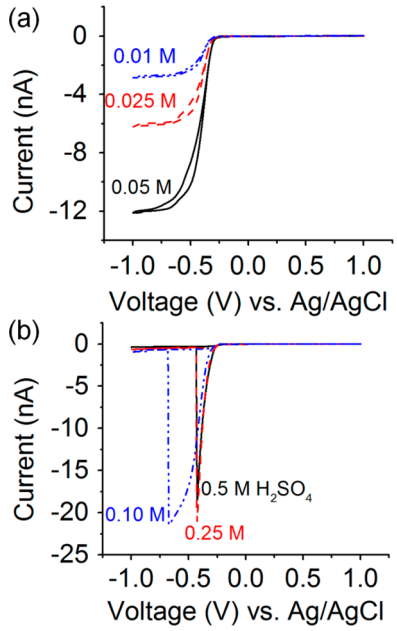

Figure 4. Cyclic voltammetric response at a 27-nm-radius Pt nanodisk as a function of H_2SO_4 solution concentration: (a) 0.01 to 0.05 M and (b) 0.1 to 0.5 M. Scan rate = 100 mV/s. The drop in current due to single nanobubble formation occurs in solutions containing greater than ~0.1 M H_2SO_4.

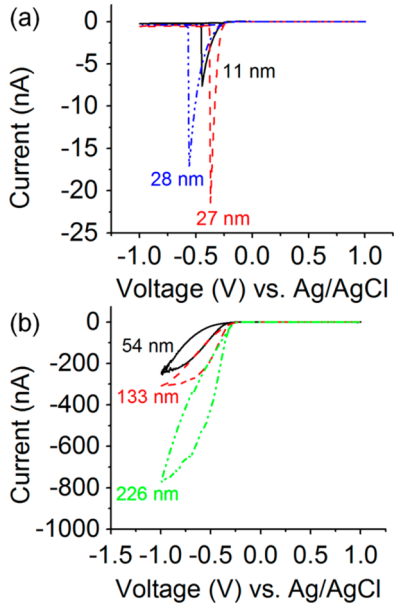

Figure 5. Cyclic voltammetric response as a function of the radius of the Pt nanodisk in a 0.5 M H_2SO_4 solution. Scan rate = 100 mV/s.

dx.doi.org/10.1021/la402496z | Langmuir 2013, 29, 11169−11175

support the formation of spherical bubbles with radii between 1 and 2 nm. The possible explanation for not seeing a drop in current is that the nanobubbles are too small to interfere significantly with the faradic current. However, the continuous formation of such small nanobubbles, which may coalesce and reduce the active electrode surface area, causes the hysteresis in the forward and reverse voltammetric scans at larger electrodes. On the basis of the present results, it is impossible to determine the size of nanobubbles formed at the larger Pt nanodisks (>50 nm) that exhibit a sigmoidal response. However, the voltammetric responses clearly indicate that nanobubbles are not large enough to cover the whole electrode surface.

Residual Current i_{nb}. After the formation of a nanobubble at the Pt nanodisk electrode, the current decreases to a residual current, i_{nb} (Figure 1a). We believe this current, corresponding to the generation of H_2, is required to balance the diffusive outflux of H_2 through the nanobubble/liquid interface, resulting in a stable nanobubble. At steady state, the diffusive flux of H_2 ($J_{H_2,d}$) through the nanobubble/liquid interface can be estimated using Fick's first law (eq 6). To simplify the calculation, the nanobubble at the electrode is assumed to be hemispherical, and $J_{H_2,d}$ is written as

$$J_{H_2,d} = -D_{H_2}\frac{dC}{dx} = -D_{H_2}\frac{C^*_{H_2} - C^s_{H_2}}{r_{nb}} \quad (6)$$

where D_{H_2} is the diffusion coefficient of H_2 (4.5×10^{-5} cm^2/s[44]) and $C^*_{H_2}$ and $C^s_{H_2}$ are the H_2 concentrations of the bulk solution and at the nanobubble/liquid interface, respectively. r_{nb} is the radius of the nanobubble, which we assume is the same as the Pt nanodisk radius (27 nm) for reasons outlined above. $C^s_{H_2}$ is estimated to be ~0.037 M from the nanobubble radius r_{nb} using Henry's law (eq 5) combined with the Young–Laplace equation (eq 4) and $J_{H_2,d}$ is ~6.2 mol/(m^2·s). Hence, the integral of $J_{H_2,d}$ over the hemispherical interface is $\sim 2.82 \times 10^{-14}$ mol/s, requiring a faradic current of ~−5.4 nA, which is ~10-fold larger than the measured residual current i_{nb} of −450 pA. The discrepancy may result from the variation of the nanobubble shape; for example, a flatter nanobubble with a larger radius of curvature has a significantly reduced inner pressure p_{nb} and thus a lower $C^s_{H_2}$ at the interface along with a reduced interfacial area. The lower $C^s_{H_2}$ and bubble surface area would result in a decrease of the total diffusive flux $J_{H_2,d}$ and, correspondingly, a smaller faradic residual current i_{nb}. (Note that on the basis of AFM images,[13] nanobubbles at the interface are typically flat instead of hemispherical on both hydrophobic and hydrophilic surfaces.) Using a similar calculation, a residual current of ~−367 pA is calculated to be required to support a flat nanobubble with a curvature of 135 nm radius that fully covers the 27-nm-radius nanodisk electrode. Additionally, Lohse et al.[17,45] proposed the cycling of the diffusive outflux of H_2 back to the nanobubble as a result of the gas attraction by the solid surface. This cycling mechanism would potentially reduce i_{nb}.

The residual current i_{nb} is provided by the electrochemical reduction of H^+. Finite element simulation was employed to investigate the transport of protons to the fraction of the Pt electrode surface not covered by the nanobubble. For simplicity, we again assume that a hemispherical nanobubble of radius r_{nb} covers the electrode, leaving just a thin ring of Pt with a width of ($a - r_{nb}$) exposed at the circumference of the nanodisk electrode. Figure 6a,b illustrates a hemispherical

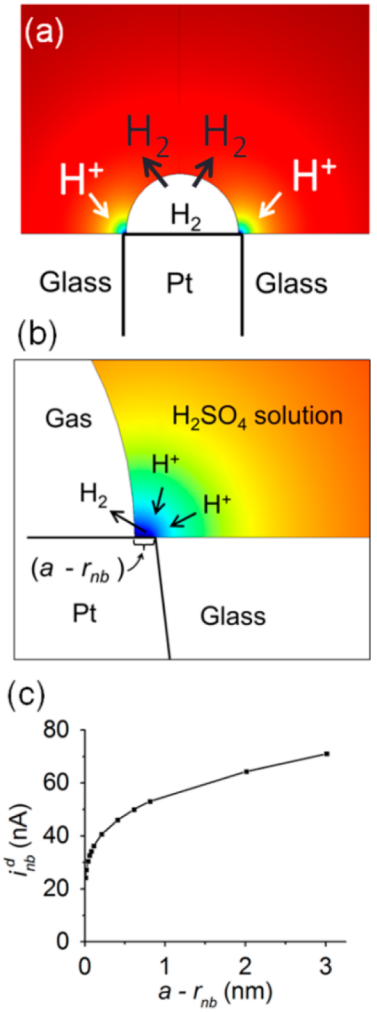

Figure 6. (a) Schematic illustration of a hemispherical nanobubble at a 27-nm-radius Pt nanodisk and the dissolution of H_2 gas into the solution balanced by the electroreduction of H^+ at the circumference of the nanobubble. The colored surface shows the distribution of H^+ under the diffusion-limited condition where the H^+ concentration is driven to zero at the Pt surface (in accordance with the Nernst equation at potentials more negative than E^o for the H^+/H_2 redox couple; dark red corresponds to 1 M H^+ far from the electrode surface). (b) Expanded illustration showing the three-phase Pt/gas/solution boundary. (c) Simulated H^+ diffusion-limited current i^d_{nb} as a function of the width of the uncovered Pt surface in part b. a is the radius of the nanodisk, and r_{nb} is the radius of the semispherical nanobubble. H^+ reduction occurs at the circumference of the Pt nanoelectrode on the exposed region of Pt defined by a ring of width ($a - r_{nb}$).

nanobubble on a 27-nm-radius Pt nanodisk at steady state, where H^+ diffuses to the Pt ring and is reduced to H_2, which enters the nanobubble at the Pt/gas/solution interface. This influx of H_2 is balanced by the outflux of H_2 at the nanobubble/liquid interface. The proton-diffusion-limited current i^d_{nb} is computed from the overall diffusive flux of H^+ to exposed area on the nanodisk where the H^+ concentration is set to 0 M. Figure 6c shows the relationship between the simulated proton-diffusion-limited current i^d_{nb} and ($a - r_{nb}$). Generally, i^d_{nb} decreases as the uncovered Pt ring width decreases as a result

dx.doi.org/10.1021/la402496z | Langmuir 2013, 29, 11169–11175

of a reduced electrode surface. However, for a ring thickness as small as 10 pm, approximately 6% of the size of a single Pt atom (175 pm[46]), the diffusion-limited current is still 24 nA, ~50 fold higher than the experimental value or ~5-fold higher than the required current estimated to balance the diffusive outflux of H_2. Therefore, it is unlikely that the diffusion of H^+ is the rate-limiting step in determining i_{nb}. Given that the diffusive flux is so large to the ring electrode, it is more likely that the current is instead limited by the adsorption and electron-transfer steps associated with H^+ reduction. It has also been reported that the current at nanoband electrodes <5 nm in width is limited by geometrical constraints associated with the comparable size of the relative redox species and the electrode.[47,48] Thus, we arrive at the conclusion that whereas a steady-state residual current for H^+ reduction is essential to maintain the nanobubble, the rate of this electrochemical reaction is limited by the adsorption and electron-transfer kinetics instead of the diffusion of the reactant (H^+).

CONCLUSIONS

This preliminary study demonstrates that the electrochemical reduction of protons in sulfuric acid solutions, using Pt electrodes with radii of less than ~50 nm, results in the formation of a single H_2 nanobubble. These individual nanobubbles are indefinitely stable as long as the electrode potential is poised sufficiently negative of the thermodynamic potential of H^+ reduction, which is necessary to balance H_2 dissolution from the nanobubble by H_2 electrogeneration at the Pt/gas/solution interface. Although electrochemical methods using Pt nanodisk electrodes appear to provide a powerful method to study individual nanobubbles, these studies raise numerous questions about the shape of the nanobubble, the relationship between the local H_2 distribution and bubble nucleation, and the role of the electrode surface properties as well as the role of the electrode/glass interface. Preliminary studies in our laboratory indicate that individual O_2 nanobubbles can also be formed at the Pt nanodisks through the electrooxidation of water, although this process is more complicated because of the sluggish kinetics of water oxidation. We are currently pursuing imaging of individual nanobubbles under electrochemical control as well as using significantly faster electrochemical instrumentation to study the dynamics of bubble nucleation. These studies will be the focus of future reports.

ASSOCIATED CONTENT

Supporting Information

Characterization of Pt nanodisk electrodes. Cyclic voltammetric response of an 11-nm-radius nanodisk electrode as a function of scan rate. Cyclic voltammetric response of an 11-nm-radius nanodisk electrode as a function of H_2SO_4 concentration. Finite element simulation of the H_2 profile at the critical current. Simulated H_2 concentration profile for a 226-nm-radius nanodisk electrode at the critical current. This material is available free of charge via the Internet at http://pubs.acs.org.

AUTHOR INFORMATION

Corresponding Author

*E-mail: white@chem.utah.edu.

Notes

The authors declare no competing financial interest.

ACKNOWLEDGMENTS

L.L. acknowledges financial support provided by a predoctoral fellowship from the University of Utah Nanotechnology Training Program. This work was supported in part by the Office of Naval Research. We thank Dr. Peter Birkin (University of Southampton) for helpful discussions.

REFERENCES

(1) Zhang, L. J.; Zhang, Y.; Zhang, X. H.; Li, Z. X.; Shen, G. X.; Ye, M.; Fan, C. H.; Fang, H. P.; Hu, J. Electrochemically Controlled Formation and Growth of Hydrogen Nanobubbles. *Langmuir* **2006**, *22*, 8109−8113.

(2) Liu, G. M.; Wu, Z. H.; Craig, V. S. J. Cleaning of Protein-Coated Surfaces Using Nanobubbles: An Investigation Using a Quartz Crystal Microbalance. *J. Phys. Chem. C* **2008**, *112*, 16748−16753.

(3) (a) Yang, S. J.; Tsai, P. C.; Kooij, E. S.; Prosperetti, A.; Zandvliet, H. J. W.; Lohse, D. Correction to Electrolytically Generated Nanobubbles on Highly Orientated Pyrolytic Graphite Surfaces. *Langmuir* **2013**, *29*, 5937−5937. (b) Yang, S. J.; Tsai, P. C.; Kooij, E. S.; Prosperetti, A.; Zandvliet, H. J. W.; Lohse, D. Electrolytically Generated Nanobubbles on Highly Orientated Pyrolytic Graphite Surfaces. *Langmuir* **2009**, *25*, 1466−1474.

(4) Lou, S. T.; Ouyang, Z. Q.; Zhang, Y.; Li, X. J.; Hu, J.; Li, M. Q.; Yang, F. J. Nanobubbles on Solid Surface Imaged by Atomic Force Microscopy. *J. Vac. Sci. Technol., B* **2000**, *18*, 2573−2575.

(5) Lou, S. T.; Gao, J. X.; Xiao, X. D.; Li, X. J.; Li, G. L.; Zhang, Y.; Li, M. Q.; Sun, J. L.; Li, X. H.; Hu, J. Studies of Nanobubbles Produced at Liquid/Solid Interfaces. *Mater. Charact.* **2002**, *48*, 211−214.

(6) Yang, J. W.; Duan, J. M.; Fornasiero, D.; Ralston, J. Very Small Bubble Formation at the Solid−Water Interface. *J. Phys. Chem. B* **2003**, *107*, 6139−6147.

(7) Zhang, X. H.; Maeda, N.; Craig, V. S. J. Physical Properties of Nanobubbles on Hydrophobic Surfaces in Water and Aqueous Solutions. *Langmuir* **2006**, *22*, 5025−5035.

(8) Switkes, M.; Ruberti, J. W. Rapid Cryofixation/Freeze Fracture for the Study of Nanobubbles at Solid−liquid Interfaces. *Appl. Phys. Lett.* **2004**, *84*, 4759−4761.

(9) Zhang, J.; Yoon, R.-H.; Mao, M.; Ducker, W. A. Effects of Degassing and Ionic Strength on AFM Force Measurements in Octadecyltrimethylammonium Chloride Solutions. *Langmuir* **2005**, *21*, 5831−5841.

(10) Zhang, X. H.; Li, G.; Maeda, N.; Hu, J. Removal of Induced Nanobubbles from Water/Graphite Interfaces by Partial Degassing. *Langmuir* **2006**, *22*, 9238−9243.

(11) Zhang, X. H.; Zhang, X. D.; Sun, J. L.; Zhang, Z. X.; Li, G.; Fang, H. P.; Xiao, X. D.; Zeng, X. C.; Hu, J. Detection of Novel Gaseous States at the Highly Oriented Pyrolytic Graphite−Water Interface. *Langmuir* **2007**, *23*, 1778−1783.

(12) van Limbeek, M. A. J.; Seddon, J. R. T. Surface Nanobubbles as a Function of Gas Type. *Langmuir* **2011**, *27*, 8694−8699.

(13) Zhang, L.; Zhang, X.; Zhang, Y.; Hu, J.; Fang, H. The Length Scales for Stable Gas Nanobubbles at Liquid/Solid Surfaces. *Soft Matter* **2010**, *6*, 4515−4519.

(14) Zhang, X. H.; Quinn, A.; Ducker, W. A. Nanobubbles at the Interface between Water and a Hydrophobic Solid. *Langmuir* **2008**, *24*, 4756−4764.

(15) Karpitschka, S.; Dietrich, E.; Seddon, J. R. T.; Zandvliet, H. J. W.; Lohse, D.; Riegler, H. Nonintrusive Optical Visualization of Surface Nanobubbles. *Phys. Rev. Lett.* **2012**, *109*, 066102.

(16) Zhang, X.; Chan, D. Y. C.; Wang, D.; Maeda, N. Stability of Interfacial Nanobubbles. *Langmuir* **2013**, *29*, 1017−1023.

(17) Brenner, M. P.; Lohse, D. Dynamic Equilibrium Mechanism for Surface Nanobubble Stabilization. *Phys. Rev. Lett.* **2008**, *101*, 214505.

(18) Ducker, W. A. Contact Angle and Stability of Interfacial Nanobubbles. *Langmuir* **2009**, *25*, 8907−8910.

(19) Weijs, J. H.; Lohse, D. Why Surface Nanobubbles Live for Hours. *Phys. Rev. Lett.* **2013**, *110*, 054501.

(20) Liu, Y.; Zhang, X. Nanobubble Stability Induced by Contact Line Pinning. *J. Chem. Phys.* **2013**, *138*, 014706.
(21) Ljunggren, S.; Eriksson, J. C. The Lifetime of a Colloid-Sized Gas Bubble in Water and the Cause of the Hydrophobic Attraction. *Colloids Surf., A* **1997**, *130*, 151−155.
(22) Das, S. Effect of Impurities in the Description of Surface Nanobubbles: Role of Nonidealities in the Surface Layer. *Phys. Rev. E* **2011**, *83*, 066315.
(23) Das, S.; Snoeijer, J. H.; Lohse, D. Effect of Impurities in Description of Surface Nanobubbles. *Phys. Rev. E* **2010**, *82*, 056310.
(24) Craig, V. S. J. Very Small Bubbles at Surfaces—The Nanobubble Puzzle. *Soft Matter* **2011**, *7*, 40−48.
(25) Zhang, X. Quartz Crystal Microbalance Study of the Interfacial Nanobubbles. *Phys. Chem. Chem. Phys.* **2008**, *10*, 6842−6848.
(26) Seddon, J. R. T.; Kooij, E. S.; Poelsema, B.; Zandvliet, H. J. W.; Lohse, D. Surface Bubble Nucleation Stability. *Phys. Rev. Lett.* **2011**, *106*, 056101.
(27) Guan, M.; Guo, W.; Gao, L.; Tang, Y.; Hu, J.; Dong, Y. Investigation on the Temperature Difference Method for Producing Nanobubbles and Their Physical Properties. *ChemPhysChem* **2012**, *13*, 2115−2118.
(28) Xiao, X.; Bard, A. J. Observing Single Nanoparticle Collisions at an Ultramicroelectrode by Electrocatalytic Amplification. *J. Am. Chem. Soc.* **2007**, *129*, 9610−9612.
(29) Xiao, X.; Fan, F.-R. F.; Zhou, J.; Bard, A. J. Current Transients in Single Nanoparticle Collision Events. *J. Am. Chem. Soc.* **2008**, *130*, 16669−16677.
(30) Kwon, S. J.; Fan, F.-R. F.; Bard, A. J. Observing Iridium Oxide (IrOx) Single Nanoparticle Collisions at Ultramicroelectrodes. *J. Am. Chem. Soc.* **2010**, *132*, 13165−13167.
(31) Zhou, H.; Fan, F.-R. F.; Bard, A. J. Observation of Discrete Au Nanoparticle Collisions by Electrocatalytic Amplification Using Pt Ultramicroelectrode Surface Modification. *J. Phys. Chem. Lett.* **2010**, *1*, 2671−2674.
(32) Zhang, B.; Galusha, J.; Shiozama, P. G.; Wang, G.; Bergren, A. J.; Jones, R. M.; White, R. J.; Ervin, E. N.; Cauley, C. C.; White, H. S. Bench-Top Method for Fabricating Glass-Sealed Nanodisk Electrodes, Glass Nanopore Electrodes, and Glass Nanopore Membranes of Controlled Size. *Anal. Chem.* **2007**, *79*, 4778−4787.
(33) Zhan, D.; Velmurugan, J.; Mirkin, M. V. Adsorption/Desorption of Hydrogen on Pt Nanoelectrodes: Evidence of Surface Diffusion and Spillover. *J. Am. Chem. Soc.* **2009**, *131*, 14756−14760.
(34) Li, Y. X.; Cox, J. T.; Zhang, B. Electrochemical Responses and Electrocatalysis at Single Au Nanoparticles. *J. Am. Chem. Soc.* **2010**, *132*, 3047−3054.
(35) Cussler, E. L. *Diffusion: Mass Transfer in Fluid Systems*, 2nd ed.; Cambridge University Press: New York, 1997.
(36) Murray, R. W. Nanoelectrochemistry: Metal Nanoparticles, Nanoelectrodes, and Nanopores. *Chem. Rev.* **2008**, *108*, 2688−2720.
(37) Cox, J. T.; Zhang, B. Nanoelectrodes: Recent Advances and New Directions. *Annu. Rev. Anal. Chem.* **2012**, *5*, 253−272.
(38) Proch, S.; Wirth, M.; White, H. S.; Anderson, S. L. Strong Effects of Cluster Size and Air Exposure on Oxygen Reduction and Carbon Oxidation Electrocatalysis by Size-Selected Pt_n ($n \geq 11$) on Glassy Carbon Electrodes. *J. Am. Chem. Soc.* **2013**, *135*, 3073−3086.
(39) Wiebe, R.; Gaddy, V. L.; Heins, C. Solubility of Hydrogen in Water at 25 °C from 25 to 1000 atm. *Ind. Eng. Chem.* **1932**, *24*, 823−825.
(40) Suggitt, R. M.; Aziz, P. M.; Wetmore, F. E. W. The Surface Tension of Aqueous Sulfuric Acid Solution at 25 °C. *J. Am. Chem. Soc.* **1949**, *71*, 676−678.
(41) Gardner, J. R.; Woods, R. The Hydrophilic Nature of Gold and Platinum. *J. Electroanal. Chem.* **1977**, *81*, 285−290.
(42) van der Niet, M. J. T. C.; den Dunnen, A.; Koper, M. T. M.; Juurlink, L. B. F. Tuning Hydrophobicity of Platinum by Small Changes in Surface Morphology. *Phys. Rev. Lett.* **2011**, *107*, 146103.
(43) van Der Niet, M. J. T.; Dunnen, C. A. Den; Juurlink, L. B. F.; Koper, M. T. M. Co-adsorption of O and H_2O on Nanostructured Platinum Surfaces: Does OH Form at Steps? *Angew. Chem.* **2010**, *122*, 6722−6725.
(44) Mazarei, A. F.; Sandall, O. C. Diffusion Coefficients for Helium, Hydrogen, and Carbon Dioxide in Water at 25°C. *AIChE J.* **1980**, *26*, 154−157.
(45) Seddon, J. R. T.; Zandvliet, H. J. W.; Lohse, D. Knudsen Gas Provides Nanobubble Stability. *Phys. Rev. Lett.* **2011**, *107*, 116101.
(46) Bondi, A. van der Waals Volumes and Radii. *J. Phys. Chem.* **1964**, *68*, 441−451.
(47) Morris, R. B.; Franta, D. J.; White, H. S. Electrochemistry at Platinum Bane Electrodes of Width Approaching Molecular Dimensions: Breakdown of Transport Equations at Very Small Electrodes. *J. Phys. Chem.* **1987**, *91*, 3559−3564.
(48) Seibold, J. D.; Scott, E. R.; White, H. S. Diffusional Transport to Nanoscopic Band Electrodes. *J. Electroanal. Chem. Interfacial Electrochem.* **1989**, *264*, 281−289.